Energy
Advances

PAPER

View Article Online
View Journal | View Issue

Cite this: *Energy Adv.*, 2024, 3, 1354

Carbon framework modification; an interesting strategy to improve the energy storage and dye adsorption†

Monika Michalska,[a] Paulina Pietrzyk-Thel,[b] Kamil Sobczak,[c] Mathijs Janssen[d] and Amrita Jain *[b]

Porous carbons find various applications, including as adsorbents for clean water production and as electrode materials in energy storage devices such as supercapacitors. While supercapacitors reach higher power densities than batteries, they are less widely used, as their energy density is lower. We present a low-temperature wet ultrasonochemical synthesis technique to modify the surface of activated carbon with 1 wt% Cu nanoparticles. We analyzed the modified carbon using X-ray diffraction, Raman spectroscopy, scanning electron microscopy, and transmission electron microscopy and confirmed the composite formation by N_2 adsorption–desorption isotherms at 77 K. For comparison, we did the same tests on pristine carbon. We used the modified carbon as an electrode material in a home-built supercapacitor filled with gel polymer electrolyte and as an absorbent of Malachite green dye. In both applications, the modified carbon performed substantially better than its pristine counterpart. The modified-carbon supercapacitor exhibited a single electrode-specific capacitance of approximately 68.9 F g^{-1}. It also demonstrated an energy density of 9.8 W h kg^{-1} and a power density of 1.4 kW kg^{-1}. These values represent improvements over the pristine-carbon supercapacitor, with increases of 25.7 F g^{-1} in capacitance, 3.8 W h kg^{-1} in energy density, and 0.5 kW kg^{-1} in power density. After 10 000 charging–discharging cycles, the capacitance of the modified-carbon supercapacitor decreased by approximately 10%, indicating good durability of the material. We found that the modified carbon's absorbance capacity for Malachite dye is more than that of the pristine carbon; the adsorption capacity value was ~153.16 mg g^{-1} for modified carbon with pseudo-second kinetic order, in accordance with the Redlich–Peterson adsorption model.

Received 7th March 2024,
Accepted 25th April 2024

DOI: 10.1039/d4ya00159a

rsc.li/energy-advances

Introduction

Ever-increasing demands for clean energy and portable water challenge materials scientists and electrochemists alike. Green energy and clean water production are two key challenges the world faces this century. Energy plays a crucial role in a country's economic growth; energy demands will increase at a higher pace, from 50% to 75%, between 2025 and 2075.[1,2] The main source of energy comes from non-renewable fossil fuel sources like coal, oil, and natural gas, generating greenhouse gases and causing climate change and global warming.[3,4] Renewable sources like solar and wind are intermittent in nature, so balancing supply and demand requires energy storage devices like batteries and supercapacitors. Better materials must be developed for these devices that, besides maximizing performance, are sustainable, durable, and non-toxic. Such new materials may find applications beyond energy storage devices; the electrode materials of supercapacitors, for example, may help desalinate seawater or absorb toxic contents from polluted streams.

Supercapacitors have attracted much attention recently because of their high power density, fast charging and discharging, and high capacitance.[5,6] These devices store energy through electric double layer-formation in electrolyte-filled porous electrodes. Both the electrolyte and electrode materials crucially affect supercapacitor performance. The liquids that fill some supercapacitors are flammable, have small potential

---

[a] *Department of Chemistry and Physico-Chemical Processes, Faculty of Materials Science and Technology, VSB-Technical University of Ostrava, 17. listopadu 2172/15, 708-00 Ostrava-Poruba, Czech Republic*

[b] *Institute of Fundamental Technological Research, Polish Academy of Sciences, Pawińskiego 5B, 02-106 Warsaw, Poland. E-mail: ajain@ippt.pan.pl*

[c] *Faculty of Chemistry, Biological and Chemical Research Centre, University of Warsaw, Żwirki i Wigury 101, 02-089 Warsaw, Poland*

[d] *Norwegian University of Life Sciences, Faculty of Science and Technology, Ås, Norway*

† Electronic supplementary information (ESI) available. See DOI: **https://doi.org/10.1039/d4ya00159a**

windows, and could leak out. A safe alternative is gel polymer electrolytes (GPEs), which entrap a liquid electrolyte in a polymer matrix. In particular, the amorphous polymer poly(vinylidene fluoride-*co*-hexafluoropropylene) (PVdF-HFP) has attracted much interest due to its high dielectric constant, thermal stability, and ability to entrap much electrolyte.

Supercapacitor electrodes are usually made from activated carbon because carbon is widely available, cheap, and has a high electrical conductivity; the high specific surface areas of activated carbons lead to high-capacitance supercapacitors.[7,8] Activated carbons are especially appealing as they can have a controlled and organised pore size distribution with high specific surface area, which makes them suitable electrode candidates.[9,10] The surface chemistry of carbon materials can be changed by post-treating them with reactive heteroatom sources. Composites of carbon with conductive polymers, metallic or metal oxide particles, or other carbon species have also been developed.[11–13] Such surface modifications can boost supercapacitor performance.[14–17]

The activated carbons of supercapacitor electrodes can also be utilised to produce clean water. Carbons can remove toxic contents from water by physical adsorption, which is more suitable and efficient than, for instance, photodegradation, photothermal conversion, and membrane technology. Physical adsorption yields fewer by-products and can be fast and highly efficient.[18] The high surface area of activated carbon gives it good adsorbing capacity for dyes.[19] Though it can adsorb most of the dyes, its adsorbing ability can still be improved, and one possible option is to make a composite with metal nanoparticles.[20] Such modification can improve the material mechanically and thermally and help develop the surface structure and morphology of the material.

The purpose of this study was to investigate the impact of surface modification with Cu nanoparticles (Cu NPs) on the surface of activated carbon (AC) and to assess its utility for energy storage and dye adsorption applications. A new low-temperature ultrasonication approach was applied for decorating AC material with Cu NPs without the use of a reducing agent. This proposed approach is simple, straightforward and cost-effective. The altered material was used to fabricate electrodes for a symmetric supercapacitor. The supercapacitor was filled with a GPE using PVdF-HFP as the host polymer, propylene carbonate (PC) as a plasticiser, and magnesium perchlorate ($Mg(ClO_4)_2$) as a salt. The electrode and electrolyte described above were employed to prepare supercapacitor cells, which were subsequently electrochemically characterised. Furthermore, the modified carbon material was evaluated as an adsorbent for dyes, specifically Malachite green in this article. This study aimed to demonstrate the effect of using only 1 wt% of copper metal nanoparticles on improving the carbon framework.

Experimental details

Preparation of activated carbon–copper composites

The activated carbon material was surface-modified using Cu nanoparticles *via* the following procedure. First, copper(II) nitrate trihydrate ($Cu(NO_3)_2 \cdot 3H_2O$, pure p.a., Sigma-Aldrich) was dissolved in 50 mL of ethanol (96%, Merck). Second, activated carbon (AC) (activated charcoal pure p.a., CHEMPUR) was added to the prepared nitrate–ethanol solution of Cu. The whole synthesis was done in an ultrasonic bath cleaner for 1 h (10 min of sonication separated by 20 min intervals). Third, the black composite was air-dried at ~60 °C and then later at ~150 °C for a few hours. Last, the activated carbon material with 1 wt% of copper was ground in an agate mortar to produce a fine composite powder. The as-prepared sample was labelled ACCu1, and a control sample without Cu nanoparticles was labelled AC. Fig. 1 schematically shows the synthesis and application.

Instrumental details

Morphological studies of ACCu1 were performed with an FEI Talos F200X scanning/transmission electron microscope (S/TEM) at 200 kV. TEM and STEM-mode measurements were recorded using a high-angle annular dark-field detector. Energy-dispersive X-ray spectroscopy (EDX) on a Brucker BD4 instrument was used to map the elements' distribution. Sample preparation for the TEM observations was done by dropping the colloidal particle dispersion on a carbon film which was supported on a 300-mesh copper grid. Scanning electron microscopy (SEM) was carried out using an SEM/FIB-Zeiss Crossbeam 350, Germany; EDX was carried out using an Ametek EDAX, Octane Elite with accelerating voltage of 7 kV to minimise the penetrating depth. X-ray powder diffraction (XRD) analysis was performed with an X-ray diffractometer of MiniFlex 600 (Rigaku, Japan) equipped with a Co tube, operated at 40 kV and 15 mA, and a DteX Ultra 250 detector. The XRD patterns of the prepared materials were collected in the 10–60° 2θ range with a step of 0.01° and a scanning rate of 10° min^{-1}. The results were evaluated using the PDXL software (Rigaku, Japan) and the PDF 2 database, which was released in 2019. The N_2 adsorption–desorption studies of the ACCu1 and AC samples were performed using an AutoSorb IQ, Quantachrome, USA, with nitrogen adsorption at 77 K. The pore size distribution curves were obtained using the built-in density functional theory (DFT) model using the adsorption branch of the isotherms. The dye adsorption experiment was carried out using a PerkinElmer (UV/VIS/NIR) Lambda 1050+ spectrophotometer. Measurements were performed in a quartz cuvette from 250 to 800 nm. Malachite green was purchased from Warchem Poland Sp. z o.o. (purity 99%), and NaCl from Sigma-Aldrich, Germany (purity > 99.9%). MilliQ-water to prepare the solutions was supplied by the Hydrolab watering system – Gliwice, Poland.

Assembly and characterization of EDLC cells

We constructed electric double-layer capacitor (EDLC) cells using magnesium ion-based GPE, which also acted as a separator, and electrodes made from the Cu-modified activated carbon. The electrodes were prepared by mixing the active materials (ACCu1 and AC) with polymeric binder (PVdF) in the ratio of 90 : 10 (wt% : wt%) using an agate pestle and mortar. Drop by drop acetone was added to obtain slurries of the

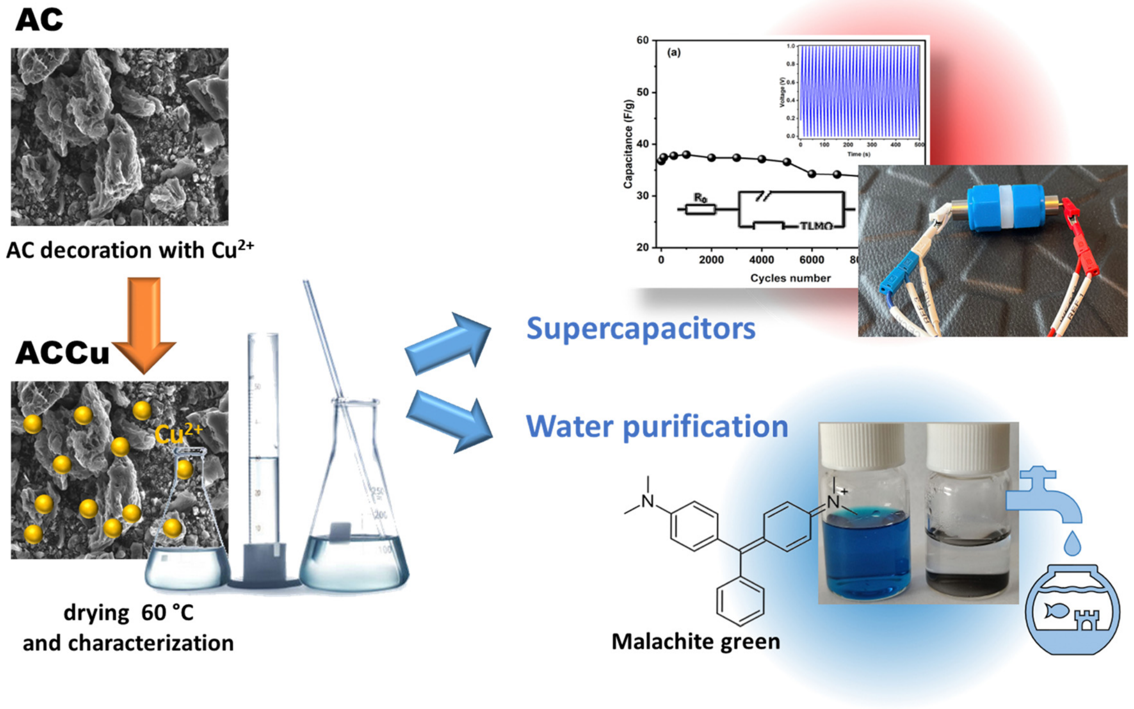

Fig. 1 Schematic of activated carbon–copper composite preparation and application.

mixtures, which were coated on carbon cloth (AVCarb, USA), which was used as the current collector. The electrodes dried at ∼100 °C for 8 h before they were used to prepare the EDLCs. The electrolyte was prepared using the host polymer poly(vinylidene fluoride-*co*-hexafluoropropylene) (PVdF-HFP), mixed with propylene carbonate (PC) as a plasticizer, magnesium perchlorate $Mg(ClO_4)_2$ was used as a salt, and tetrahydrofuran (THF) as a solvent. All materials were purchased from Merck and were used as received. Details of the electrolyte preparation and characterization are discussed elsewhere.[21]

EDLC cells were prepared by sandwiching the GPE between the prepared electrodes as shown below:

Cell A: ACCu1|GPE film|ACCu1

Cell B: AC|GPE film|AC

The area of the electrodes was set to 1 cm^2, and the mass of the active materials was ∼1.5 mg. The electrochemical performance of both prepared EDLCs was characterized by electrochemical impedance spectroscopy (EIS), cyclic voltammetry (CV), and galvanostatic charge–discharge (GCD) cycles, all under ambient conditions. The electrochemical measurements were carried out using a Biologic VMP3 (France) electrochemical workstation. The EIS measurements were carried out between 200 kHz and 1 mHz at an applied amplitude of 5 mV. The CV experiments were performed in the 0–1.0 V range at scan rates of 1, 5, 10, 20, 50, and 100 mV s^{-1}. The GCD measurements were conducted with current densities between 0.1 and 0.6 A g^{-1}. The cyclic performance was analysed using the GCD method at a constant current density of 1 A g^{-1} in between 0 to 1.0 V. We used eqn (S1)–(S4) of the ESI† to calculate specific capacitance (C_{sp}), energy density, and power density from the different techniques.

Adsorption studies

Next, we explored the potential of the ACCu1 material for adsorption applications, for instance, to remove toxic chemicals from a solution. Measurements were performed using 20 mL of fresh Malachite green (MG) dye solutions with a concentration of 20 mg L^{-1} (54.8 μmol). As adsorption depends on multiple parameters, we measured different contact times, mass, pH, and ionic strength to determine the optimal conditions. Furthermore, to understand the adsorption mechanism, kinetic studies were performed, and isotherms were estimated. The surveys were recorded by varying the mass from 2.5 mg to 10 mg, contact time from 1 min to 30 min, and interrupt effects like pH from 2–10 and ionic strength from 0.04 to 0.20 mol L^{-1} concentration of NaCl solution. The amount of adsorbed dye (Q) on the carbon surface was calculated using eqn (S5) and (S6) of the ESI.†

Results and discussion

Characteristics of the prepared carbon composites

Fig. 2a shows a TEM image of the ACCu1 material, with a zoomed-in view in the right panel. The figure shows a typical amorphous carbon structure. We investigated the distribution of copper in the porous carbon matrix by EDX. Fig. 2b shows

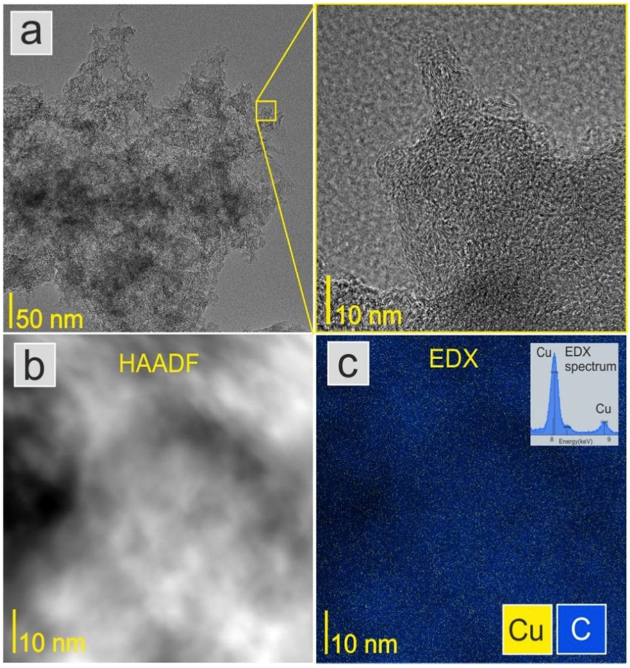

Fig. 2 (a) TEM image of the surface-modified activated carbon (ACCu1), with a zoomed-in view showing a typical amorphous carbon structure. (b) HAADF image and (c) Cu and C distribution map with the EDX spectrum in the Cu energy region.

the high-angle annular dark-field (HAADF) imaging results, with the corresponding EDX map of the Cu and C elements in Fig. 2c (with EDX spectrum in the Cu energy window). These data show the presence of Cu atoms, or at most Cu atomic clusters. No particles larger than a nanometer can be observed.

Fig. 3a shows the morphology of the activated carbon modified with copper nanoparticles. As can be seen from the image, the material is dense and amorphous. This kind of morphology is suitable for the electrode material for supercapacitor applications. The EDX spectra of the ACCu1 sample are provided in the ESI† (Fig. S1); from that analysis, the presence of copper particles is confirmed. Fig. 3b shows the XRD pattern of the ACCu1 sample. This pattern has diffraction peaks around 2θ values of 31 and 51°, matching the crystal planes of (002) and (100) of the graphite (PDF card: 03-065-6212) phase, respectively. The peak around 51° is caused by overlapping phases of graphite (100) and Cu (111). The diffraction line around 59° corresponds to the crystal plane of (200) of the copper phase. The XRD pattern of the pristine AC material was presented in our previous work.[22]

Fig. 3c shows Raman spectra for the ACCu1 and AC samples. The spectra have bands at ~1334, ~1587, ~2688, and ~2920 cm^{-1}, which matches the D, G, 2D, and D + G bands of the typical graphitic materials, respectively. The bands (D, G, 2D, D + G) are in almost the same position as in previous works, and their attribution is similar. To support the structural results, the Raman spectroscopy measurements were investigated. Fig. 3c shows Raman spectra for the ACCu1 and AC samples. Due to the prevalence of sp^3 hybridization in the carbon structure and the E$_{2g}$ phonon vibrations of the sp^2

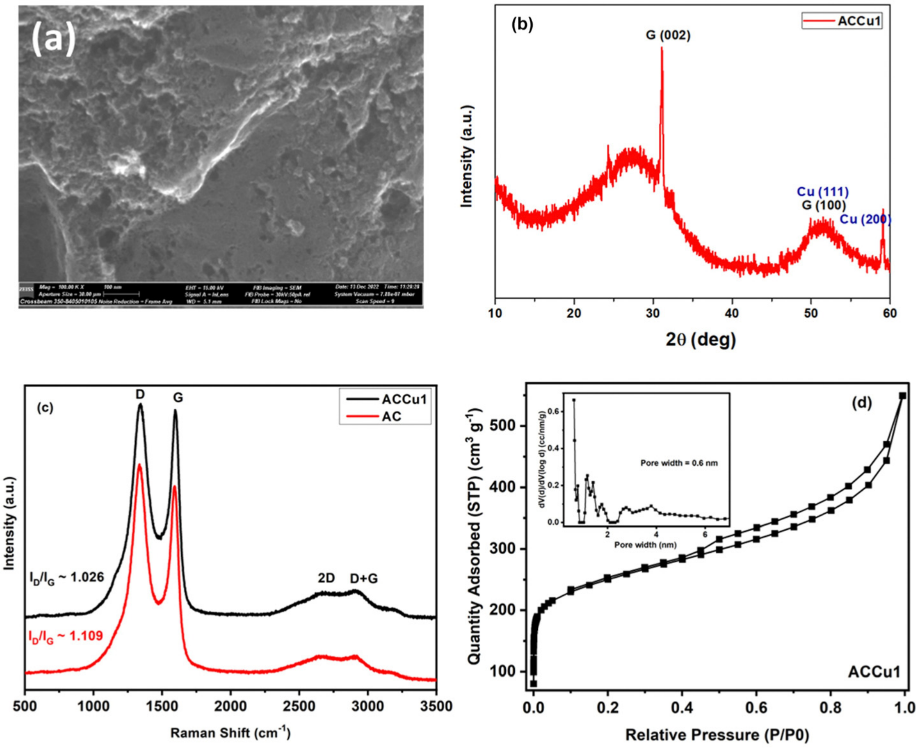

Fig. 3 (a) SEM image of ACCu1. (b) XRD spectrum of ACCu1. (c) Raman spectra of surface-modified carbon (ACCu1) and commercial carbon (AC). (d) N$_2$ adsorption–desorption isotherm of ACCu1; inset: pore size distribution curve of ACCu1.

Table 1 Specific surface area and pore parameters of the prepared samples

Samples	S_{BET} (m^2 g^{-1})	V_{micro} (cm^3 g^{-1})	V_{meso} (cm^3 g^{-1})	V_{total} (cm^3 g^{-1})	D_0 (nm)
ACCu1	893.6	0.16	0.69	0.85	3.1
AC	657.6	0.12	0.5	0.62	3.8

Note: S_{BET}, specific surface area; V_{micro}, micropore volume; V_{meso}, mesopore volume; V_{total}, total volume and D_0, average pore width.

carbon atoms, the D and G bands are associated with the A_{1g} vibrational mode of the disordered carbon structure. The scattering of phonons near the zone boundary (*K*-point) forms the second-order vibration of the G-mode, referred to as the 2D-mode. The presence of defects in the graphitic structure is indicated by the D + G band linking the D and G bands.[22,23] Considering the degree of graphitization, which suggests the crystallinity level of carbon materials in the present case, the ratio of the intensity lines (I_D/I_G) for ACCu1 and AC was found to be 1.026 and 1.109, respectively. Furthermore, the I_D/I_G ratio decreases most probably due to the reason for our novel low-temperature chemical method that has been proposed to surface modify the activated carbon material with copper metallic nanoparticles. Similar observations regarding the decrease in I_D/I_G ratio have been noticed in our previous works.[22,23]

Fig. 3d and Fig. S2 (ESI†) show N_2 adsorption–desorption isotherms of ACCu1 and AC, respectively, with corresponding pore-size distribution curves as insets (calculated using the DFT method). The isotherm of commercial carbon follows a type I curve, confirming its microporous structure. Meanwhile, the isotherm of ACCu1 follows a type IV pattern, wherein we have observed a small hysteresis loop in the relative pressure range in between 0.4–1.0, which confirms the mesoporous characteristics of the material with a capillary condensation phenomenon. Hence, the mesoporous nature of carbon increases after adding copper. However, the ACCu1 isotherms rise in the low-pressure region ($P/P_0 < 0.03$), showing that the ACCu1 composite also contains micropores. Hence, ACCu1 has a mixture of micropores and mesopores, which is beneficial for energy storage and dye adsorption applications. Table 1 lists the values of specific surface area, micro, meso, and macro pore volumes, and pore sizes of the ACCu1 and AC materials resulting from the adsorption–desorption spectra. Both materials are composed of a mixture of micropores and mesopores. However, the volume of the micropores in ACCu1 is lower than that of the mesopores, which is preferable in the present case. The high surface area and mesoporous structure probably relieve slight changes in the material's volume during the charge–discharge process, providing better pathways for electrolyte transport.[24] This phenomenon may also be the reason for our novel low-temperature chemical method involving an ultrasonication process that has been proposed to surface modify the activated carbon material with copper metallic nanoparticles. Our method enables the deposition of metal nanoparticles on the grains of the material to be modified, rather than becoming embedded in the pores of the material like other chemical methods used to modify the surface of materials with metallic coatings/layers/nanoparticles. Similar observations regarding the increase in BET surface area were found in our previous works.[22,23] The pore size distribution curves further confirm the co-existence of micropores, mesopores, and macropores. As per the literature, micropores enhance the electrochemical double-layer capacitance, mesopores can decrease the ion-transport resistance, and macropores minimize the diffusion distances.[25–27] In the present case, ACCu1 has a good balance of pores and a pore structure beneficial for electrolyte transfer. Moreover, the copper in the carbon structure provides abundant active sites, giving superior electrochemical and dye adsorption properties; hence, it is chosen as an electrode and adsorbate material.

Electrochemical characterization of EDLC cells

The electrochemical evaluation of ACCu1 and AC was investigated using CV, EIS, and GCD tests in a two-electrode configuration. Fig. 4a shows cell A and B's CV curves at a scan rate of 5 mV s^{-1} at room temperature. Box-type or rectangular-type shapes have been observed for both cells with varying covering areas. The CV curve of cell A spans a larger area than that of cell B, which confirms the superior performance of cell A over B, and the capacitance of cell A (C = 64.8 F g^{-1}) is higher than that of cell B (C = 46.8 F g^{-1}), accordingly. The higher capacitance value shows that the modification of carbon with copper has increased the material's overall conductivity and mesoporosity, which enhanced its electrochemical performance. An optimum meso-to-microporosity ratio provides porous pathways to electrolyte ions, *i.e.*, facile insertion/de-insertion of electrolyte ions (Mg^{2+} and ClO_4^- in the existing system) for double-layer formation. Fig. 4b shows CV curves of cell A for scan rates from 1 mV s^{-1} to 100 mV s^{-1} in between 0 to 1 V. Cell A has box-like or rectangular-like CV curves up to 50 mV s^{-1}, confirming the fast and easy switching of the ions (Mg^{2+} and ClO_4^-). Beyond 100 mV s^{-1}, the CV curves become less rectangular, showing less capacitance of ∼27.5 F g^{-1}. To evaluate the optimal potential stability range of cell A, the CV of cell A has been recorded with voltage limits of 1.0 V to 1.4 V, see Fig. 4c. The CV curves have symmetrical box-type shapes until 1.2 V. Later, their shapes cease to be rectangular, indicating that the cell is electrochemically stable up to 1.2 V. Hence, the rest of the electrochemical studies were conducted in the range from 0 to 1.0 V for safety operation of the device. The working voltage range is also confirmed by GCD studies discussed below.

Fig. 4d shows how the specific capacitance of cell A varies with the scan rate between 1 mV s^{-1} to 100 mV s^{-1}. The capacitance decreases fast at first and more gradually later. An increased ion adsorption and mass transfer may cause the capacitance to decrease at high scan rates, and the electric double layer may have been gathered over a relatively shorter distance. As a result, ions do not properly settle inside or within

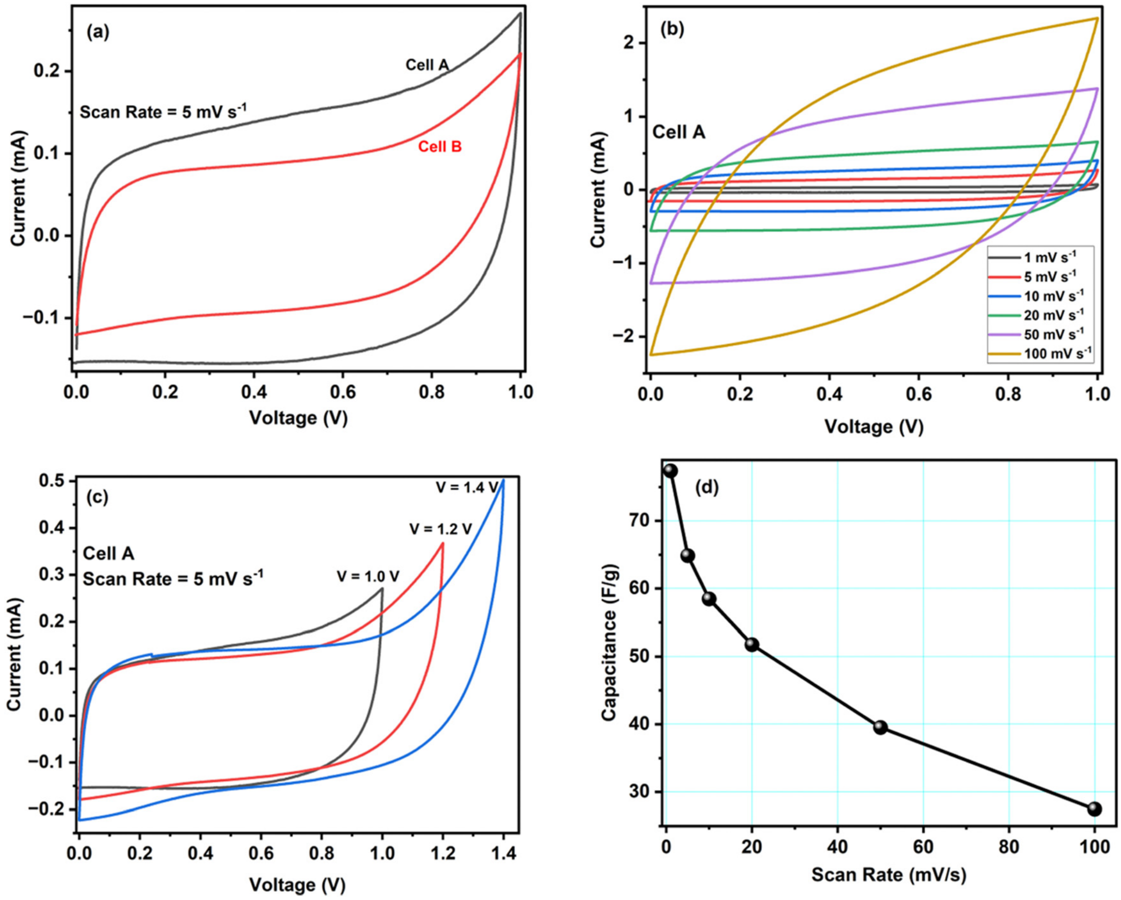

Fig. 4 (a) Cell A and B CV curves at a scan rate of 5 mV s^{-1}. (b) CV curves of cell A at different scan rates. (c) CV curves of cell A at a scan rate of 5 mV s^{-1} for different maximal voltages. (d) Scan-rate dependence of cell A's specific capacitance.

the pores of the electrode material, and the capacitance decreases. On the contrary, at lower values of scan rate, the mass transport of ions is relatively slower at the electrode–electrolyte interface.[28] Therefore, all the ions can easily diffuse inside the pores, enhancing charge storage and specific capacitance.

Next, we characterised cells A and B by electrochemical impedance spectroscopy in the frequency range from 1 mHz to 200 kHz. Fig. 5 and Fig. S3 (ESI†) present results for cells A and B, respectively (we used the lin-KK method of the impedance.py package[29] to check the validity of these data). Both figures contain a complex-plane impedance plot (a), a zoomed-in view of the high frequencies regime (b), and the frequency dependence of Re(Z) and Im(Z) (c). The complex plane plots of both cells show the following features: (1) at low frequencies, the cells have a phase angle of about 80 degrees; that is, they deviate substantially from a pure capacitance. (2) At intermediate frequencies, the Nyquist plots have phase angles around

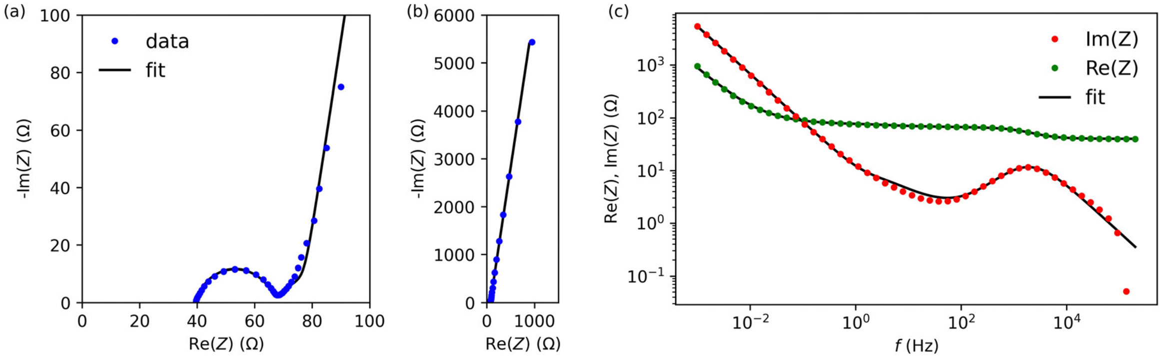

Fig. 5 Impedance spectroscopy data for cell A. (a) Complex plane impedance plot. (b) Zoomed-in view of the high-frequency regime of panel (a). (c) The real and imaginary part of the impedance *versus* frequency.

Table 2 Electrical parameters of EDLC cells from EIS analysis

	Cell A	Cell B
R_0	4.00×10^1 ($\pm 4.40 \times 10^0$) [Ω]	4.44×10^1 ($\pm 3.93 \times 10^0$) [Ω]
Q	6.37×10^{-6} ($\pm 1.66 \times 10^{-5}$) [$\Omega^{-1}s^{a}$]	8.94×10^{-6} ($\pm 4.79 \times 10^{-6}$) [$\Omega^{-1}s^{a}$]
a	9.25×10^{-1} ($\pm 2.90 \times 10^{-1}$) [—]	7.78×10^{-1} ($\pm 6.30 \times 10^{-2}$) [—]
R_1	2.56×10^1 ($\pm 6.37 \times 10^0$) [Ω]	1.10×10^2 ($\pm 6.13 \times 10^0$) [Ω]
R_{ion}	3.24×10^1 ($\pm 1.57 \times 10^1$) [Ω]	1.10×10^2 ($\pm 1.53 \times 10^1$) [Ω]
Q_{s}	1.80×10^{-2} ($\pm 9.69 \times 10^{-5}$) [F $s^{\gamma-1}$]	1.05×10^{-2} ($\pm 2.90 \times 10^{-5}$) [F $s^{\gamma-1}$]
γ	9.05×10^{-1} ($\pm 1.06 \times 10^{-3}$) [—]	9.09×10^{-1} ($\pm 5.99 \times 10^{-4}$) [—]

(but larger than) that of the Warburg impedance (45 degrees). (3) There is a high-frequency arc. This arc is slightly depressed; its apex lies lower than half its base width.

To create an equivalent circuit model for both cells, we note that observations (1) and (2) suggest using a finite-length Warburg open impedance, modified with a CPE-like parameter to fit the low frequencies, $Z_{\text{TLMQ}}(R_{\text{ion}}, Q_{\text{s}}, \gamma) = \sqrt{\frac{R_{\text{ion}}}{Q_{\text{s}}(i\omega)^{\gamma}}}\coth\sqrt{R_{\text{ion}}Q_{\text{s}}(i\omega)^{\gamma}}$. Here, we note that using a finite-length Warburg element is natural in the case of a porous electrode with finite-length pores. Correcting the low-frequency phase angle of the Warburg open impedance by a CPE parameter was done previously by ref. 30 and 31. Next, the high-frequency depressed arc can be modelled by a CPE, $Z_{\text{CPE}}(Q, a) = \frac{1}{Q(i\omega)^{a}}$, in parallel with resistor R_1. Interfacial redox reactions of impurities or surface functionalities at the carbon surface may have caused this arc.[28] However, the high-frequency arcs do not need to be caused by a charge transfer. If a pore has a narrow entrance, narrower than the rest of the pore, this may also lead to an impedance curve of a similar shape.[32] Finally, at the highest frequencies, we measure the electrolyte resistance R_0 of the bulk electrolyte between the two electrodes. We connect the above circuit elements into the following Randles-like circuit:

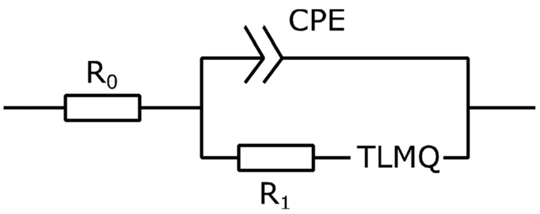

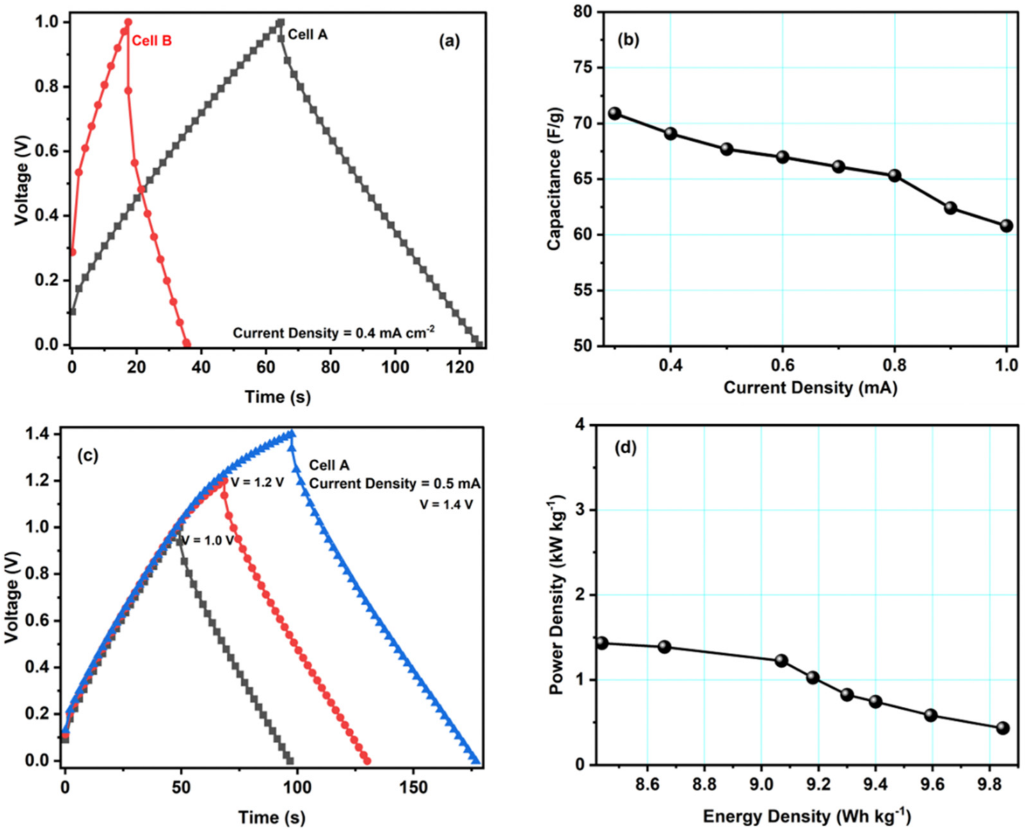

Fig. 6 (a) GCD measurements of cells A and B at a current density of 0.4 mA cm^{-2}. (b) Variation of the specific capacitance of cell A with current density. (c) Variation of the GCD curves of cell A with voltage at a current density of 0.5 mA cm^{-2}. (d) Ragone plot of cell A.

Table 3 Summary of the various parameters obtained from GCD studies

Cell	Discharge capacitance values (C_d) [F g^{-1}]	ESR Ω cm^2	Energy density (E) [W h kg^{-1}]	Power density (P) [kW kg^{-1}]
A	66.9	297.5	9.8	1.4
B	43.2	871.8	6.0	0.9

We fit this circuit to the EIS data using the impedance.py package.[29] This package makes a non-linear least squares fit with uniform weighting; see the package documentation for details. We observe a decent correspondence between the fits and the data in Fig. 5 and Fig. S3 (ESI†). The ESI† discusses how the circuit can be extended for even better fits.

Table 2 reports the fit parameters and their standard variation. We see that the bulk resistance is roughly the same in both cells, which makes sense as we used the same electrolyte and cell layout in both cases. Next, cell A has lower R_1 and R_{ion} resistances than cell B, which reinforces our earlier observation that the ACCu1 electrode of cell A has a lower internal electrolyte resistance. The capacitance-like Q_s parameter is also higher for this cell, further suggesting that the modification of carbon with copper improved the electrochemical properties of the material.

Galvanostatic charge–discharge (GCD) tests have also been carried out for cells A–B to calculate their specific capacitance, energy and power density values. Fig. 6a shows GCD curves for cells A and B, recorded at a current density of 0.4 mA cm^{-2}. The figure shows an almost triangular-shaped GCD pattern for cell A, which confirms that the charge storage is purely due to electrical double-layer formation and not because of the pseudocapacitance. We determined the equivalent series resistance ESR = $\Delta V/2I$ by applying the sudden voltage drop (ΔV) in the discharge curve, leading to the constant current I. Table 3 lists the ESR and specific capacitances of cells A and B. These data show that cell A has a lower ESR and a higher capacitance, in accordance with the results obtained with other techniques like CV and EIS. Hence, the GCD study further confirms that the modification of carbon with copper enhances the electrochemical performance of the material.

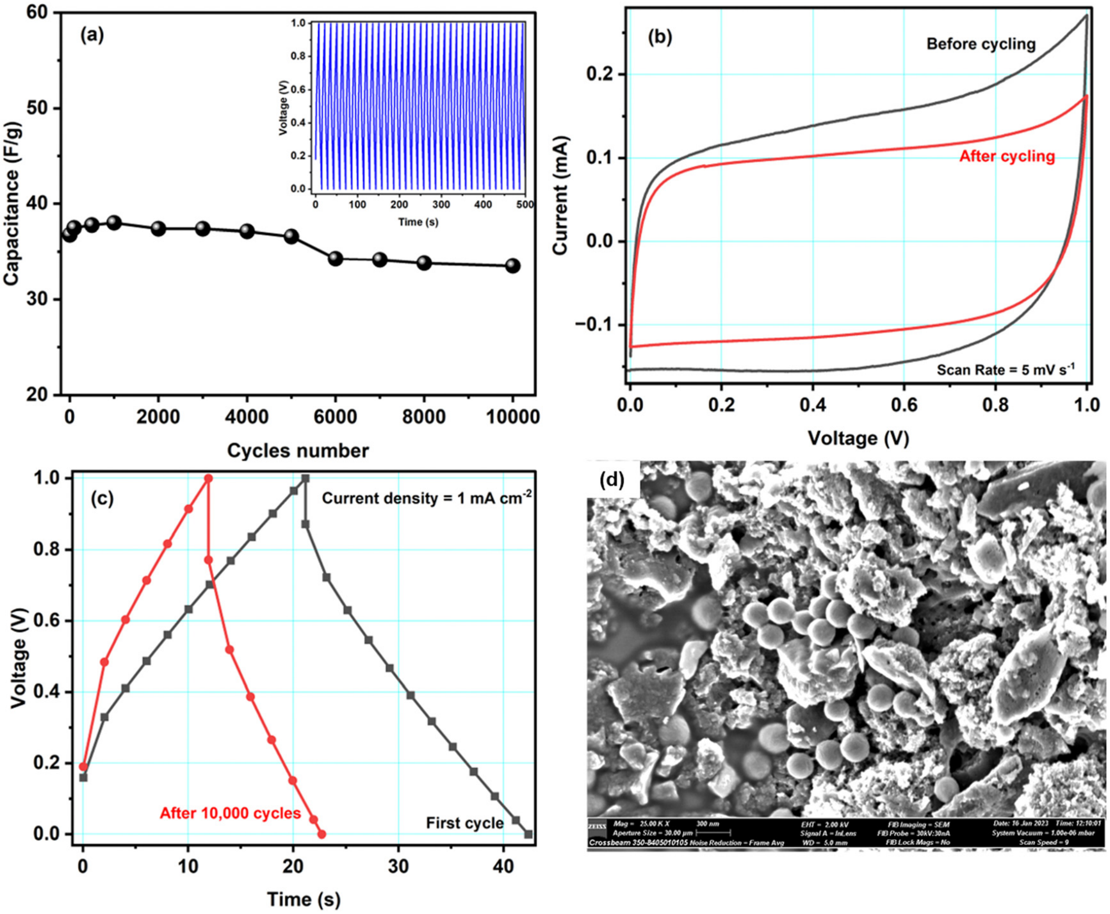

Fig. 7 (a) Variation of specific capacitance of cell A with the number of GCD cycles. The inset of (a) shows the first five hundred GCD cycles. (b) and (c) Comparison of the CV and GCD curves before and after 10 000 cycles and (d) SEM image of the ACCu1 electrode after 10 000 cycles.

Table 4 Comparison of other carbon-based materials for symmetric supercapacitors

Electrode material	Capacitance (F g^{-1})	Power density (kW kg^{-1})	Energy density (W h kg^{-1})	Cycle stabilisation	Ref.
Pinecone	43	0.454	16.1	10 000	38
Rotten potato	54	0.524	20.8	5000	39
AC@Co	66	15		10 000	40
Carbon aerogels	21	1.9	11.5	3000	41
Rotted cucurbita pepo-derived activated carbon	55	0.176	14.98	8000	42
Mango seeds	28.17	0.375	35.21	6000	43
Activated carbon + Fe_3O_4	54.4	1.2	4.7	10 000	44
ACCu1	68.9	1.4	9.8	10 000	This work

Fig. 6b shows the specific discharge capacitance for different current densities. The figure shows that cell A's specific capacitance decreases with increasing current density, possibly due to the ion adsorption and mass transfer, which reduced the mobility of ions at the electrode–electrolyte interfaces due to high current values. GCD studies for voltages from 1.0 V to 1.4 V also revealed the maximum operating voltage range to agree with the CV studies. As can be seen, up to 1.4 V, the triangular pattern of the curves is maintained (Fig. 6c). Hence, the safer limit of the prepared cell is up to 1.4 V. This agrees with the CV measurements discussed above.

Fig. 6d presents cell A's Ragone plot (specific energy density values *versus* specific power density values). The plot clearly shows that the energy density of cell A depreciates with the increment in the power density values. Here, the energy density varies from 9.8 W h kg^{-1} to 8.4 W h kg^{-1}, and the power density varies from 1.4 to 0.4 kW kg^{-1}. These values are similar to other EDLC/supercapacitor cells reported in the literature.[33–37]

Fig. 7a shows the specific capacitance of cell A during ~10 000 charge–discharge cycles recorded at a current density of 1.6 mA cm^{-2} at 1.0 V. During the first 100 cycles, the capacitance was unstable, possibly due to irreversible electrochemical reactions at the electrode–electrolyte interface. Later, the cell was stable. Overall, cell A had excellent cyclability as it retained ~91% of its capacitance after 10 000 cycles. We did not observe substantial structural changes in the active material, so the slight decrease in the capacitance may have been caused by micropores being blocked by ions, which is supported by scanning electron microscopy performed on the electrode after cycling (discussed below). The inset of Fig. 7a shows the first fifty GCD cycles of cell A. The GCD curves kept their triangular shape with good repeatability.

Fig. 7b and c show CV curves at the scan rate of 5 mV s^{-1} and GCD curves at a current density of 1 mA cm^{-2} before and after 10 000 GCD cycles. Both figures show slight differences in the respective curves. As mentioned above, the capacitance decreased by about 10%. However, even after 10 000 cycles, the cell is working properly. Hence, the Cu-modified carbon material shows great promise as an electrode material. To get further insight into cell A's cyclability, SEM images with EDX spectra of the cycled electrode were obtained, see Fig. 7d. The SEM images before and after cycling show no significant

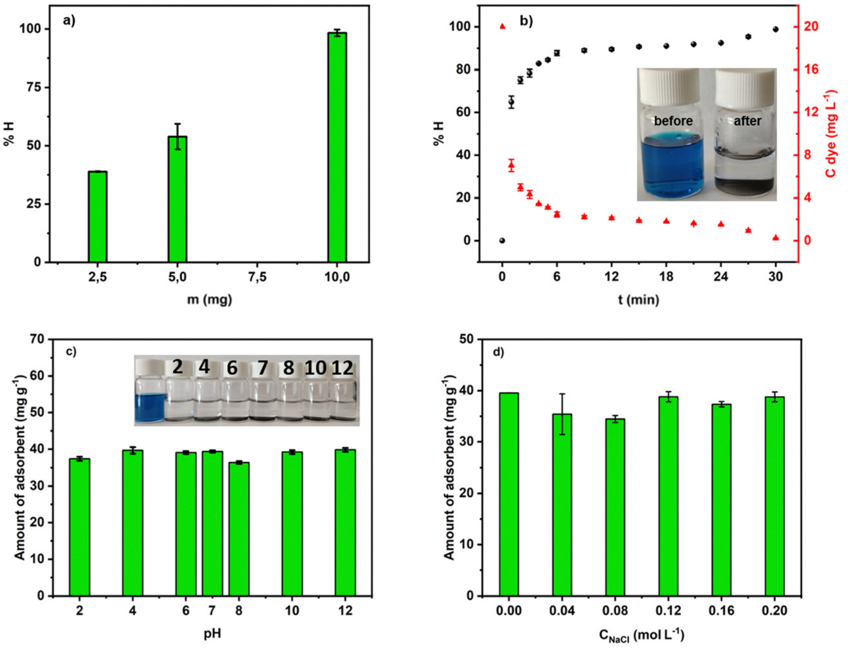

Fig. 8 (a) Mass effect in the removal of MG into aqueous solution at pH 7; (b) efficiency of the adsorption process at pH 7; (c) and (d) effect of pH and ionic strength.

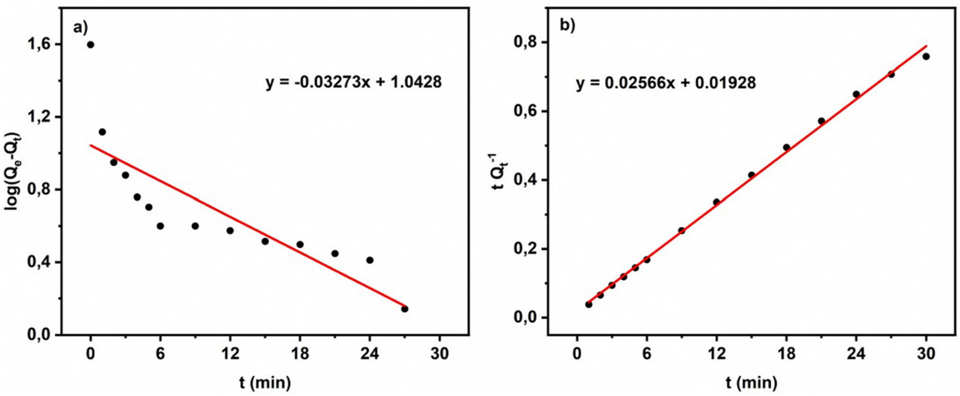

Fig. 9 Kinetic orders for the adsorption process of MG by ACCu1: (a) pseudo-first order, (b) pseudo-second-order.

Table 5 Kinetic parameters of the MG adsorption process

Material	k_1 (min^{-1}) × 10^{-3}	$Q_{\text{ecal.}}$ (mg g^{-1})	R^2	k_2 (g mg^{-1} min^{-1})	$Q_{\text{ecal.}}$ (mg g^{-1})	$Q_{\text{exp.}}$ (mg g^{-1})	R^2
AC Cu	14.212	11.036	0.6692	78.774	38.971	38.162	0.9977

difference. Some small spheres were observed, which might appear from magnesium salt or polymer from the electrolyte material. From the EDX studies, shown in Fig. S4 in the ESI,† it is also clear that, after cycling, the traces of Mg, F, Cl, O, *etc.* have been found in the electrode sample, which is clearly because of the interaction of the electrode and electrolyte during electrochemical testing of the cell. Some ions might get stuck in the electrode's pores, which would explain the observed decrease in capacitance. The literature comparison of other carbon-based materials for symmetric supercapacitors is presented in Table 4. It is important to underline that in our work we proposed an easy, straightforward and cost-effective method for depositing Cu NPs on activated carbon surface without the use of reducing agent. Furthermore, in this study we have also fabricated a symmetrical supercapacitor cell comprising ACCu1, in which the gel polymer electrolyte is immersed. This is the first time that this particular cell configuration has been examined.

Dye adsorption studies

Effect of mass and removal of dye. First, weight optimization of the ACCu1 sample was carried out. For that, 2.5 mg, 5 mg, and 10 mg of ACCu1 were added to the 20 mL dye solution, respectively, and the solution was magnetically stirred for 15 s. After this, the solution was equilibrated for 30 min at room temperature, and then the samples were centrifuged for ∼2–3 s, followed by UV spectra measurements. Fig. 8a shows the effectiveness of the adsorption process, where 2.5 mg, 5 mg, and 10 mg of ACCu1 removed 7.77 ppm, 10.78 ppm, and 19.66 ppm, respectively. 10 mg of active material removed the most dye, so we used this sample for further measurements of the effect of pH, ionic strength, and kinetics.

Fig. 8b depicts the efficiency of MG removal *versus* time. In about 4 min, more than 80% of the dye was adsorbed. Within 30 min, ACCu1 eliminated 98.68% (9.77 ppm) of the dye. Hence, ACCu1 has excellent potential to remove this toxic dye. The inset of Fig. 8b shows the solution before and after the adsorption process.

Effect of pH and ionic strength. The pH strongly affects the distribution of surface charging and the adsorbent's adsorption capacity.[45] We prepared solutions with pH from 2 to 12 to investigate how pH affects the adsorption of MG. Interestingly, the effectiveness of MG dye removal by ACCu1 was over 95% in the whole pH range (see Fig. 8c). In acidic and alkaline solutions, the amount adsorbed was about 37.46 mg g^{-1} and 39.82 mg g^{-1}, respectively. The highest value of %*H* was obtained at pH 7 (19.64 ppm); hence, this pH was used for further analysis. Fig. 8d shows the effect of ionic strength on the amount adsorbed. The adsorption capacity decreases

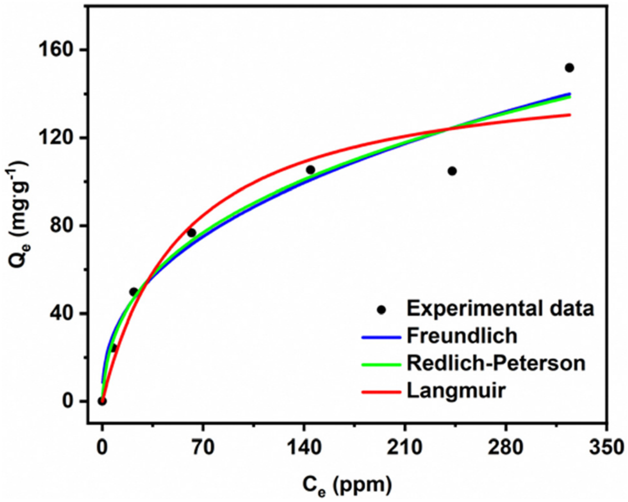

Fig. 10 Adsorption isotherm for MG dye removal.

Table 6 Fitting parameters from isotherm studies

Langmuir		Freundlich		Redlich-Peterson	
$Q_{\max}$ (mg g^{-1})	153.16	K_F (mg g^{-1} (mg $L^{-1})^{-1/nF}$)	13.327	g (L g^{-1})	0.6487
K_L (L mg^{-1})	0.0177	n	2.4576	K_{RP}	13.824
R^2	0.9298	R^2	0.9248	a_{RP} (mg $L^{-1})^{-g}$	0.7363
				R^2	0.9453

slightly with increasing the salt concentration up to the lowest value at ~0.08 mol L^{-1}, where the concentration of MG in the solution is higher, about 1.05 ppm (% H = 92.97%). However, the removal of MG is kept at more than 92%. Concluding, neither the pH of the solution nor the presence of NaCl ions affects dye removal by ACCu1 substantially.

Kinetic study. Kinetic studies were carried out to understand the adsorption effectiveness. Fig. 9 shows the linear presentation of kinetic models. Specifically, Fig. 9a shows that the diffusion pseudo-first order follows the Langergen model and the pseudo-second-order follows the McKay–Ho model. The Langergen model shows that a pollutant-sorbent complex is formed in the active centre in the adsorbent structure.[46] However, the McKay–Ho model assumes that the adsorption process occurs because of chemisorption.[47] The equations used to calculate pseudo-first and pseudo-second order kinetics are given in the ESI† Sections (S7 and S8), and the values of different parameters are in Table 5.

Comparing the R^2 values of the kinetic model fits, the process of MG adsorption by ACCu1 follows pseudo-second-order kinetics. The value of the experimental adsorption capacity is close to the calculated capacity, which confirms the equilibrium. The pseudo-second-order constant has a higher value, showing that MG adsorption on the ACCu1 surface is very fast, consistent with the obtained experimental data.

Isotherm study. Adsorption isotherm studies provide information on the interaction between adsorbent and adsorbate. Experiments were performed using MG solutions with concentrations between 20 and 400 ppm. We determined the maximum adsorption capacity using the Langmuir, Freundlich, and Redlich–Peterson models; the corresponding eqn (S9)–(S11) are in the ESI.† The Langmuir model confirms the formation of a monolayer on the adsorbate's surface, and the adsorption rate is proportional to the number of available active sites.[36,48] However, the Freundlich model assumes the possibility of the formation of multilayers with their uneven distribution on the adsorbate surface.[49] Meanwhile, the Redlich–Peterson model combines the Langmuir and Freundlich models; hence, it could be applied over wide ranges of adsorbate concentration.[50,51]

Fig. 10 shows that Q_e increases with increasing MG concentration. The figure also shows the fits of the non-linear isotherm models to our experimental data; Table 5 presents the corresponding fit parameters. We see there that the Redlich–Peterson model has a higher R^2 coefficient (R^2 = 0.9453) than the Langmuir and Freundlich (having almost identical values, R^2 = 0.9298 and R^2 = 0.9248). Hence, the Redlich–Peterson model provides a slightly better fit.

We found an adsorption capacity of 153.16 mg g^{-1} using the Langmuir eqn (S10) (ESI†). The value of the heterogeneity factor ($n > 1$) confirms that the adsorption process is favourable in the present case.

The dimensionless g factor of the Redlich–Peterson model lies between 0 and 1. In our case, it is equal to 0.6487 (Table 6), which shows that the Redlich–Peterson model describes the adsorption process of MG dye on the ACCu1 sample well. In Table S1 (ESI†), a comparison of the adsorption capacity with different adsorbents has been summarised by using MG dye.

Conclusion

By a low-temperature wet ultrasonochemical method that was both simple, economical and environmentally friendly, we modified the surface of activated carbon with Cu nanoparticles. We used this material, ACCu1, as an electrode material in a home-built supercapacitor and as an adsorbent of Malachite green dye. In both these applications, ACCu1 performed substantially better than its pristine carbon counterpart. The supercapacitor with ACCu1 electrodes had a specific capacitance of ~68.9 F g^{-1}, an energy density of 9.8 W h kg^{-1}, and a power density of 1.4 kW kg^{-1}; this was 43.2 F g^{-1}, 6.0 W h kg^{-1}, and 0.9 kW kg^{-1}, respectively, for the pristine-carbon counterpart. After 10 000 consecutive charge–discharge cycles, the capacitance had dropped by only 10% proving the durability of ACCu1 as an electrode material. The adsorption studies performed with ACCu1 showed that, within 6 minutes, more than 80% of the Malachite dye was removed; after 30 minutes, the system was close to equilibrium. The adsorption process was of pseudo-second kinetic order. The Redlich–Peterson model fitted well to the obtained experimental data. The adsorption capacitance for MG was 153.16 mg g^{-1}, which is higher than reported in the literature for other materials. ACCu1 is thus a multifunctional composite material with great potential in supercapacitor development and water-purification applications.

Data availability

The data that support the findings of this study are available from the corresponding author upon reasonable request.

Author contributions

Monika Michalska: conceptualization, methodology, formal analysis, investigation, writing – original draft, writing – review and editing, visualization, supervision, funding acquisition. Paulina Pietrzyk-Thel: conceptualization, methodology, formal analysis, investigation, writing – original draft, writing – review and editing, visualization. Kamil Sobczak: formal analysis, investigation, writing – original draft. Mathijs Janssen: formal analysis, investigation, writing – original draft, writing – review and editing, resources. Amrita Jain: conceptualization, methodology, formal analysis, investigation, writing – original draft, writing – review and editing, resources, visualization, funding acquisition.

Conflicts of interest

The authors declare that they have no known competing financial interests or personal relationships that could have appeared to influence the work reported in this paper.

Acknowledgements

We thank Dr Magdalena Osial (IPPT PAN) for UV-Vis spectroscopic measurements, Dr Kamil Bochenek (IPPT PAN) for SEM measurements and Dr Vlastimil Matejka (VSB-TUO) for XRD measurements of the ACCu1 sample. This work was financially supported by the National Centre for Research and Development (NCBR, Poland); Project number: V4-Japan/2/17/AtomDeC/2022 and the Ministry of Education, Youth and Sports, Czech Republic (contract no. 8F21007) under the Visegrad Group-Japan 2021 Joint Call on Advanced Materials in cooperation with the International Visegrad Fund. M. J. was supported by a FRIPRO grant from The Research Council of Norway (Project No. 345079).

References

1 V. Thavasi, G. Singh and S. Ramakrishna, *Energy Environ. Sci.*, 2008, **1**, 205.

2 M. M. Mekonnen and A. Y. Hoekstra, *Sci. Adv.*, 2016, **2**(2), DOI: **10.1126/sciadv.1500323**.

3 M. Ge, C. Cao, J. Huang, S. Li, Z. Chen, K.-Q. Zhang, S. S. Al-Deyab and Y. Lai, *J. Mater. Chem. A*, 2016, **4**, 6772–6801.

4 K. Aruchamy, K. Dharmalingam, C. W. Lee, D. Mondal and N. Sanna Kotrappanavar, *Chem. Eng. J.*, 2022, **427**, 131477.

5 K. Samdhyan, P. Chand, H. Anand and S. Saini, *J. Energy Storage*, 2022, **46**, 103886.

6 J. Sun, C. Liu, X. Song, J. Zhang, Y. Liu, L. Liang, R. Jiang and C. Yuan, *Appl. Phys. Rev.*, 2022, **9**, 031301.

7 D. Wang, J. Nai, H. Li, L. Xu and Y. Wang, *Carbon*, 2019, **141**, 40–49.

8 D. Wang, S. Liu, L. Jiao and G. Fang, *Electrochim. Acta*, 2017, **252**, 109–118.

9 A. Shokry, M. Karim, M. Khalil, S. Ebrahim and J. El Nady, *Sci. Rep.*, 2022, **12**, 11278.

10 Z. Zhai, L. Zhang, T. Du, B. Ren, Y. Xu, S. Wang, J. Miao and Z. Liu, *Mater. Des.*, 2022, **221**, 111017.

11 S. Wang, Z. Hu, Z. Pan and D. Wang, *J. Alloys Compd.*, 2021, **876**, 160203.

12 R. Yuksel, O. Buyukcakir, P. K. Panda, S. H. Lee, Y. Jiang, D. Singh, S. Hansen, R. Adelung, Y. K. Mishra, R. Ahuja and R. S. Ruoff, *Adv. Funct. Mater.*, 2020, **30**(10), 1909725.

13 F. Schütt, S. Signetti, H. Krüger, S. Röder, D. Smazna, S. Kaps, S. N. Gorb, Y. K. Mishra, N. M. Pugno and R. Adelung, *Nat. Commun.*, 2017, **8**, 1215.

14 S. Kour, S. Tanwar and A. L. Sharma, *J. Alloys Compd.*, 2022, **910**, 164834.

15 A. Kumar, H. K. Rathore, D. Sarkar and A. Shukla, *Electrochem. Sci. Adv.*, 2021, **2**(6), e2100187.

16 Y. Teng, K. Liu, R. Liu, Z. Yang, L. Wang, H. Jiang, R. Ding and E. Liu, *Mater. Res. Bull.*, 2017, **89**, 33–41.

17 L. Zhang, S. L. Candelaria, J. Tian, Y. Li, Y. Huang and G. Cao, *J. Power Sources*, 2013, **236**, 215–223.

18 Z. Liu, X. Huang, Y. Miao, B. Gao, Y. Shi, J. Zhao and S. H. Tan, *Ind. Crops Prod.*, 2022, **187**, 115510.

19 Z. Sun, K. Qu, J. Li, S. Yang, B. Yuan, Z. Huang and Z. Guo, *Adv. Compos. Hybrid Mater.*, 2021, **4**, 1413–1424.

20 A. Q. Alorabi, M. Shamshi Hassan and M. Azizi, *Arabian J. Chem.*, 2020, **13**, 8080–8091.

21 S. K. Tripathi, A. Jain, A. Gupta and M. Mishra, *J. Solid State Electrochem.*, 2012, **16**, 1799–1806.

22 A. Jain, M. Michalska, A. Zaszczyńska and P. Denis, *J. Energy Storage*, 2022, **54**, 105367.

23 A. Jain, M. Ghosh, M. Krajewski, S. Kurungot and M. Michalska, *J. Energy Storage*, 2021, **34**, 102178.

24 G. Wang, M. Zhang, L. Lu, H. Xu, Z. Xiao, S. Liu, S. Gao and Z. Yu, *ChemNanoMat*, 2018, **4**, 964–971.

25 Y. Li, Z. Fu and B. Su, *Adv. Funct. Mater.*, 2012, **22**, 4634–4667.

26 Q. Zhao, X. Wang, C. Wu, J. Liu, H. Wang, J. Gao, Y. Zhang and H. Shu, *J. Power Sources*, 2014, **254**, 10–17.

27 Y. Lv, L. Gan, M. Liu, W. Xiong, Z. Xu, D. Zhu and D. S. Wright, *J. Power Sources*, 2012, **209**, 152–157.

28 Mohit, N. Yadav and S. A. Hashmi, *J. Energy Storage*, 2022, **55**, 105421.

29 M. Murbach, B. Gerwe, N. Dawson-Elli and L. Tsui, *J. Open Source Software*, 2020, **5**, 2349.

30 J. Landesfeind, J. Hattendorff, A. Ehrl, W. A. Wall and H. A. Gasteiger, *J. Electrochem. Soc.*, 2016, **163**, A1373–A1387.

31 A. Lasia, *Electrochemical Impedance Spectroscopy and its Applications*, Springer New York, New York, NY, 2014, pp. 85–125.

32 H. Keiser, K. D. Beccu and M. A. Gutjahr, *Electrochim. Acta*, 1976, **21**, 539–543.

33 N. M. Santhosh, K. K. Upadhyay, G. Filipič, J. Zavašnik, M. de Fátima Montemor and U. Cvelbar, *Carbon*, 2023, **203**, 686–694.

34 R. Rohith, A. T. Prasannakumar, R. R. Mohan, V. Manju and S. J. Varma, *ChemistrySelect*, 2022, **7**(41), e202203068.

35 M. F. Koudahi and E. Frąckowiak, *Energy Storage Mater.*, 2022, **49**, 255–267.

36 K. Subhani, N. Hameed, A. Al-Qatatsheh, J. Ince, P. J. Mahon, A. Lau and N. V. Salim, *J. Energy Storage*, 2022, **56**, 105936.

37 A. Jain, S. R. Manippady, R. Tang, H. Nishihara, K. Sobczak, V. Matejka and M. Michalska, *Sci. Rep.*, 2022, **12**, 21024.

38 M. Rajesh, R. Manikandan, S. Park, B. C. Kim, W. Cho, K. H. Yu and C. J. Raj, *Int. J. Energy Res.*, 2020, **44**, 8591–8605.

39 A. Wang, K. Sun, R. Xu, Y. Sun and J. Jiang, *J. Clean Prod.*, 2021, **283**, 125385.

40 K. A. Abdullin, M. T. Gabdullin, Z. K. Kalkozova, S. T. Nurbolat and M. Mirzaeian, *Energies*, 2023, **16**, 4287.

41 H. D. Asfaw, A. Kucernak, E. S. Greenhalgh and M. S. P. Shaffer, *Compos. Sci. Technol.*, 2023, **238**, 110042.

42 S. Peng, Y. Wu, S. Lu, R. Zhao, L. Dai, B. Chen, Q. Xie and Y. Ruan, *Diam. Relat. Mater.*, 2024, **141**, 110646.

43 S. Lu, W. Yang, M. Zhou, L. Qiu, B. Tao, Q. Zhao, X. Wang, L. Zhang, Q. Xie and Y. Ruan, *J. Colloid Interface Sci.*, 2022, **610**, 1088–1099.

44 A. Witecka, P. Pietrzyk-Thel, M. Krajewski, K. Sobczak, A. Wolska and A. Jain, *J. Alloys Compd.*, 2024, **985**, 174040.

45 L. B. Carvalho, P. M. B. Chagas, T. R. Marques, A. Razafitianamaharavo, M. Pelletier, P. Nolis, C. Jaime, S. S. Thomasi and L. D. M. A. Pinto, *J. Environ. Chem. Eng.*, 2019, **7**, 103492.

46 M. Marković, M. Gorgievski, N. Štrbac, V. Grekulović, K. Božinović, M. Zdravković and M. Vuković, *Metals*, 2023, **13**, 206.

47 Y. S. Ho and G. McKay, *Process Biochem.*, 1999, **34**, 451–465.

48 M. J. Ahmed and S. K. Dhedan, *Fluid Phase Equilib.*, 2012, **317**, 9–14.

49 M. Yadav and N. K. Singh, *Appl. Water Sci.*, 2017, **7**, 4793–4800.

50 K. Y. Foo and B. H. Hameed, *Chem. Eng. J.*, 2010, **156**, 2–10.

51 K. Vasanth Kumar, M. M. de Castro, M. Martinez-Escandell, M. Molina-Sabio, J. Silvestre-Albero and F. Rodriguez-Reinoso, *Chem. Phys. Lett.*, 2010, **492**, 187–192.